JOURNAL OF SOLID STATE CHEMISTRY 92, 116–129 (1991)

Metal–Insulator Transition and Thermoelectric Properties in the System $(R_{1-x}Ca_x)MnO_{3-\delta}$ (R: Tb, Ho, Y)

T. KOBAYASHI, H. TAKIZAWA*, T. ENDO, T. SATO, AND M. SHIMADA

Department of Molecular Chemistry and Engineering, Faculty of Engineering, Tohoku University, Aoba-ku, Sendai, Miyagi 980, Japan

AND H. TAGUCHI AND M. NAGAO

Research Laboratory for Surface Science, Faculty of Science, Okayama University, Okayama 700, Japan

Received July 24, 1990; in revised form December 26,1990

$(R_{1-x}Ca_x)MnO_{3-\delta}$ (R: Tb, Ho, Y) solid solutions with the orthorhombic perovskite-type structure were synthesized and their electrical resistivity and thermoelectric power were measured in the temperature range 80 to 1000 K. At low temperature, the electrical properties of $(R_{1-x}Ca_x)MnO_{3-\delta}$ are explained by the variable range hopping of electrons model. At high temperature, hopping conduction occurs in the composition range $0.4 \leqq x \leqq 0.6$, while metal–insulator transition occurs in the range $0.7 \leqq x \leqq 0.9$. Transition temperature increases with increasing average Mn–O distance. It is concluded that the increase in Mn–O distance enhances the magnitude of the electrostatic field, and consequently the transition temperature is raised. $(R_{1-x}Ca_x)MnO_{3-\delta}$ (R: Tb, Ho, Y, $0.7 \leqq x \leqq 0.9$) are candidates as high temperature thermoelectric conversion materials.

Introduction

Metal–insulator transitions in the perovskite systems have been widely investigated. $R_{1-x}Sr_xCoO_3$ (R: Nd, Pr) and $LaNi_{1-x}M_xO_3$ (M: Cr, Mn, Fe, Co) solid solutions show composition-controlled metal–insulator transitions (*1–3*), while $LaCoO_3$ shows a temperature-induced metal–insulator transition (*4*). In the latter case, the transition occurs as a result of temperature-dependent compositional change of diamagnetic and paramagnetic cobalt species (*4*).

The electrical properties of the system $(R_{1-x}Ca_x)MnO_{3-\delta}$ (R: La, Nd, Gd) have been investigated (*5–7*). These manganates exhibit *n*-type semiconducting behavior below room temperature. The electrical resistivity follows the Mott $T^{-1/4}$ law, indicating the possible occurrence of variable range hopping of electrons due to Anderson localization (*8,9*). At high temperature, metal–insulator transition occurs without a change in the crystallographic parameters. It was reported that the metal–insulator transition was caused by a change in the spin state of trivalent manganese ion (*6, 7*). The metal–insulator transition temperature decreases with the decreasing ionic radius of the rare earth ions.

In the present study, the solid solution

0022-4596/91 $3.00

system $(R_{1-x}Ca_x)MnO_{3-\delta}$ containing rare earth ions (Tb^{3+}, Ho^{3+}, and Y^{3+}) of smaller ionic radii than those of La^{3+}, Nd^{3+}, and Gd^{3+} were synthesized and electrical resistivity was measured in order to study the correlation between lattice distortion and metal–insulator transition. Thermoelectric properties were also investigated and their potentials as high temperature thermoelectric conversion materials were examined.

Experimental

All $(R_{1-x}Ca_x)MnO_{3-\delta}$ (R:Tb, Ho, Y) compounds were prepared by a standard ceramic technique. Powders of $CaCO_3$, $MnCO_3$, and rare earth metal oxides were weighed in the appropriate proportions and milled for 48 hr with acetone. After the mixed powders were dried at 100°C, they were calcined at 850°C for 15 hr in air. The calcined powders were ground and pressed into pellet form under a pressure of 100 MPa, and then the pellets were heated at 1350–1400°C for 24 hr under a stream of pure oxygen gas. The oxygen-deficient materials obtained in this way were annealed at 700°C for 12 hr under pure oxygen gas.

The phases of the products were identified by X-ray powder diffraction analysis using Ni-filtered Cu$K\alpha$ radiation. The lattice parameters were determined by a least-squares method using silicon as an internal standard. The oxygen content in each sample was determined by the oxidation–reduction method (*10*).

The electrical resistivity was measured by a standard four-electrode technique in the temperature range 80 to 1000 K. The thermoelectric power was measured using thermocouples as contacts in the temperature range 80 to 1000 K by applying a temperature gradient along the length of a sample ranging from 5 to 10°C. Cu/Constantan and Pt/Pt–13%Rh thermocouples were used below and above room temperature, respectively. Copper or platinum metal was used as an electrode. The values of thermoelectric power were obtained from the slope of temperature difference versus thermoelectromotive force.

Results and Discussion

1. Synthesis of the Perovskite-Type Solid Solution

X-ray powder diffraction patterns of $(R_{1-x}Ca_x)MnO_{3-\delta}$ (R: Ho, Y) were completely indexed as the orthorhombic perovskite-type ($GdFeO_3$-type) structure in the composition range $0.5 \leqq x \leqq 1.0$. In the composition range $x < 0.5$, a hexagonal perovskite-type phase coexisted with the orthorhombic phase. Complete series of solid solution with the orthorhombic perovskite-type structure were formed in the $(Tb_{1-x}Ca_x)MnO_{3-\delta}$ system. The oxygen content of $(R_{1-x}Ca_x)MnO_{3-\delta}$ (R: Tb, Ho, Y) annealed at 700°C under pure oxygen was determined to be 2.97–2.98 (δ: 0.02–0.03) from the chemical analysis, and independent of the composition.

Compositional dependences of the lattice parameters of $(R_{1-x}Ca_x)MnO_{3-\delta}$ (R: Tb, Ho, Y) are shown in Fig. 1. It was reported that the lattice parameters of $(R_{1-x}Ca_x)MnO_{3-\delta}$ (R: Nd, La), in which the ionic radius of Nd^{3+} and La^{3+} were close to that of Ca^{2+}, were monotonously decreased with increasing x (*6, 7*). Such linear decrease is explained by the increase of Mn^{4+} content; that is, the ionic radius of the Mn^{4+} is smaller than that of Mn^{3+} located at the octahedral site. In the present solid solution systems containing an ionic radius of R^{3+} smaller than that of Ca^{2+}, the unit cell volume linearly decreases with increasing x. Both the a-axis and the b-axis decrease with increasing x, while the c-axis has a maximum value at about $x = 0.8$. The second anomalous change in the c-axis observed in $(Tb_{1-x}Ca_x)MnO_{2.98}$ ($x < 0.5$) may be due to the Jahn–Teller effect of the Mn^{3+} located at the octahedral site.

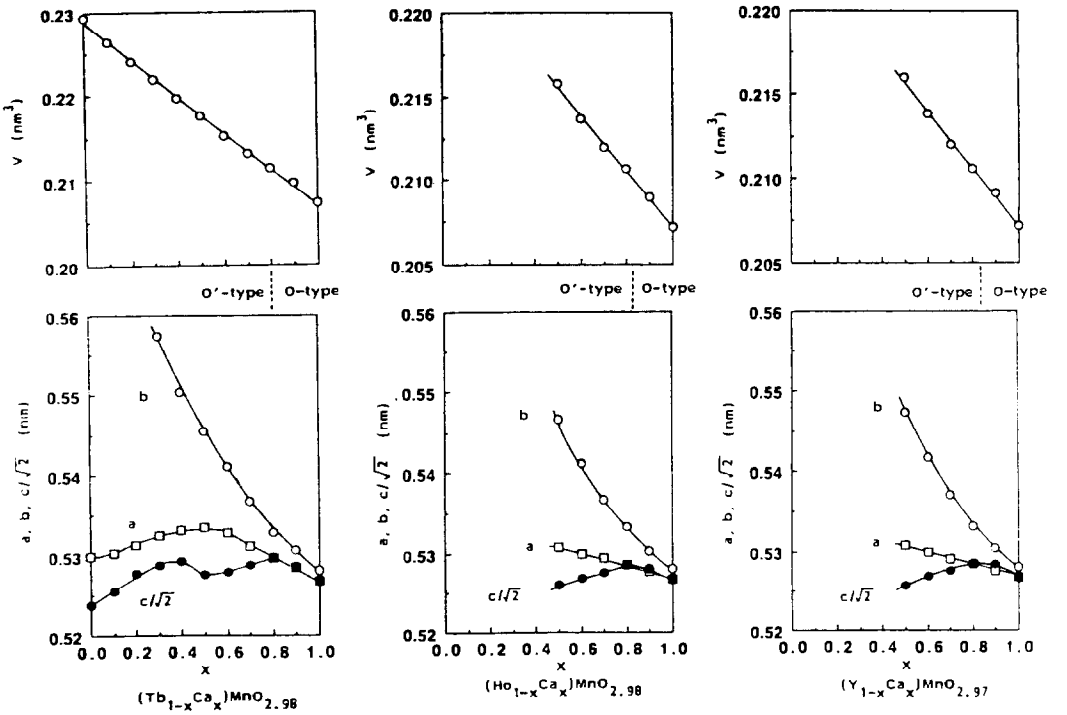

FIG. 1. Compositional dependences of the lattice parameters of $(R_{1-x}Ca_x)MnO_{3-\delta}$ (R: Tb, Ho, Y).

Two types of orthorhombic structures, the O-type ($a \doteqdot c/\sqrt{2} < b$) and the O′-type ($a < c/\sqrt{2} < b$), are distinguished for all solid solution systems as shown in Fig. 1. The *O*-type structure was also formed in the $(Nd_{1-x}Ca_x)MnO_{2.99}$ ($0.5 \leqq x \leqq 1.0$) and $(La_{1-x}Ca_x)MnO_{2.97}$ ($0.8 \leqq x \leqq 1.0$) systems (*6, 11*). It is well known that the difference in symmetry of the perovskite-type structure is explained by the tolerance factor ($t = (r_A + r_B)/\sqrt{2}(r_B + r_X)$ for ABX_3) proposed by Goldschmidt (*12*). A cubic perovskite-type structure is stable if the parameter t is equal to unity. If t is slightly different from unity, the perovskite structure is slightly distorted. Figure 2 shows the variation of the tolerance factor with the composition for various $(R_{1-x}Ca_x)MnO_{3-\delta}$ systems. The tolerance factor was calculated by using Ahrens' ionic radii (*13*). The arithmetical average of the ionic radii were taken for an *A*-site cation ($R_{1-x}Ca_x$). The boundary between the O-type and the O′-type orthorhombic structures was determined to be $t = 0.860$ from the present results. This critical value is consistent with the results of

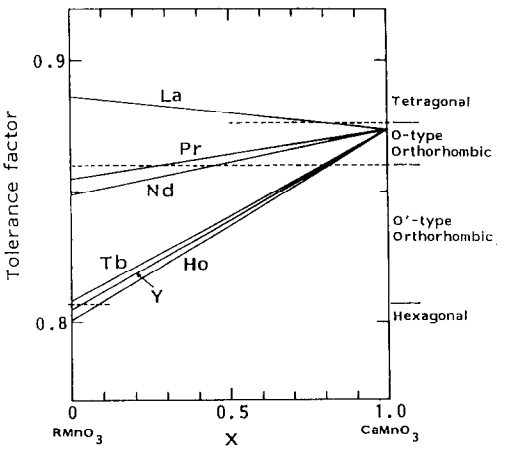

FIG. 2. The variation of the tolerance factor with the composition in the system $(R_{1-x}Ca_x)MnO_{3-\delta}$ (R: rare earth element).

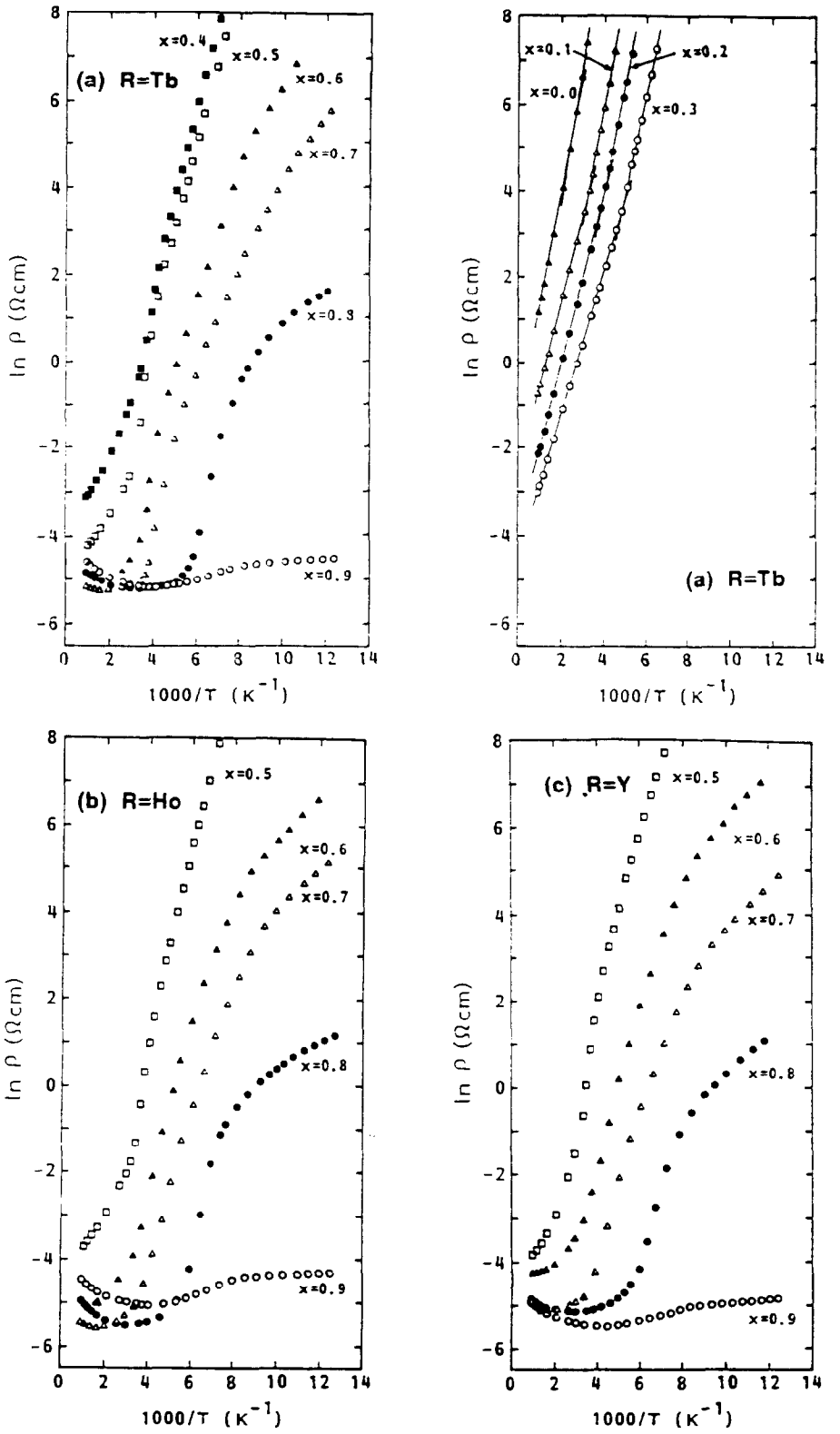

FIG. 3. $\ln \rho$ vs $1/T$ plots of $(R_{1-x}Ca_x)MnO_{3-\delta}$ (R: Tb, Ho, Y).

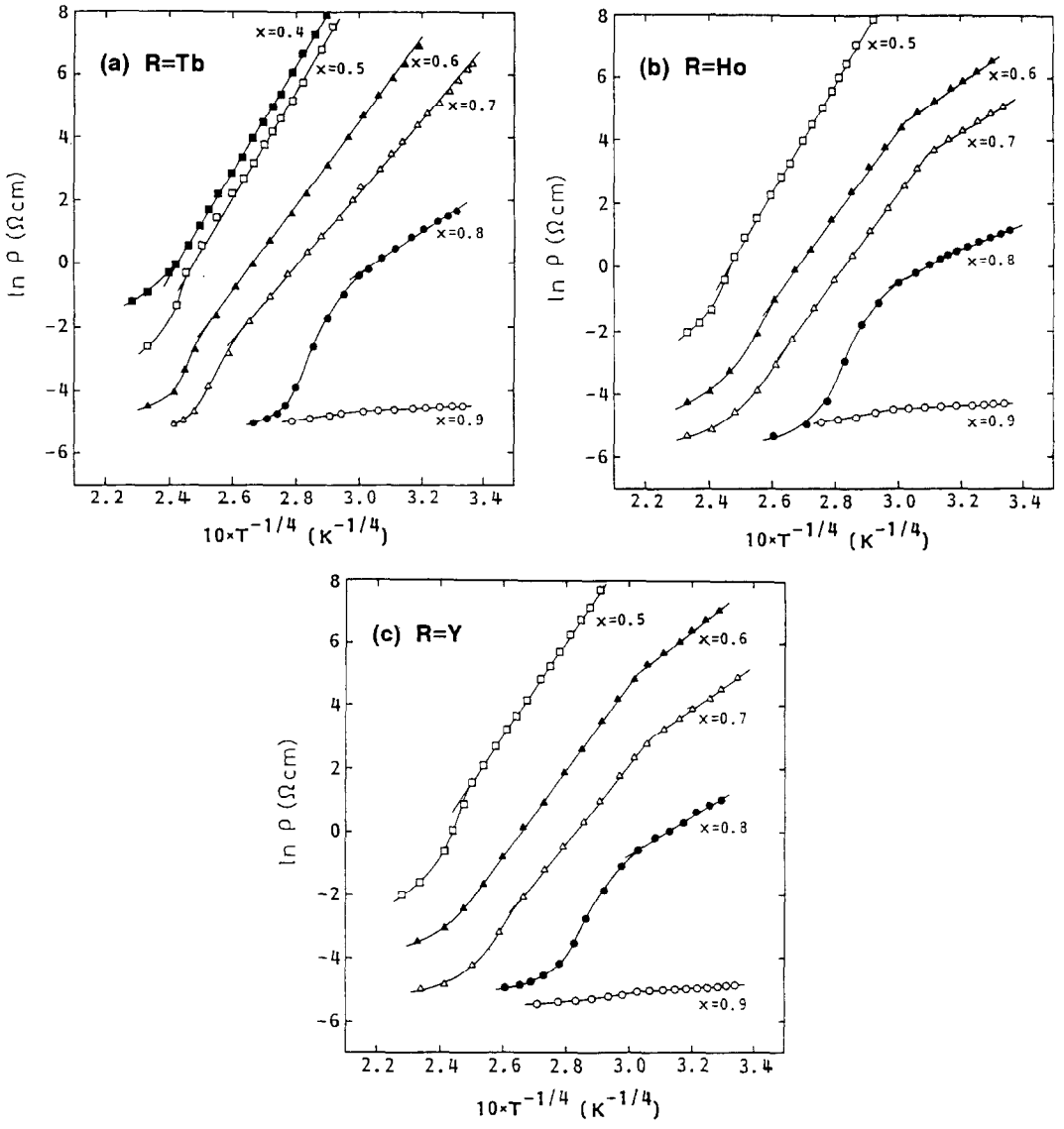

FIG. 4. ln ρ vs $T^{-1/4}$ plots of $(R_{1-x}Ca_x)MnO_{3-\delta}$ (R: Tb, Ho, Y).

$(Nd_{1-x}Ca_x)MnO_{2.99}$ (*6*) and $(Pr_{1-x}Ca_x)MnO_3$ (*14*) systems. The tetragonal–orthorhombic (O-type) boundary was determined from the results of the $(La_{1-x}Ca_x)MnO_{2.97}$ system (*11*) and also indicated in Fig. 2.

2. *Metal–Insulator Transition*

The results of the electrical resistivity measurements are shown in Fig. 3. Below room temperature, all $(R_{1-x}Ca_x)MnO_{3-\delta}$ (R: Tb, Ho, Y) samples are semiconductors with a negative temperature coefficient of resistivity and the electrical resistivity decreases with increasing x. The relation between ln ρ and $1000/T$ is not linear in the low temperature region, except $(Tb_{1-x}Ca_x)MnO_{2.98}$ ($0 \leqq x \leqq 0.3$). The relation of ln ρ vs $T^{-1/4}$ in $(R_{1-x}Ca_x)MnO_{3-\delta}$ is shown in Fig. 4. At low temperature, ln ρ follows the

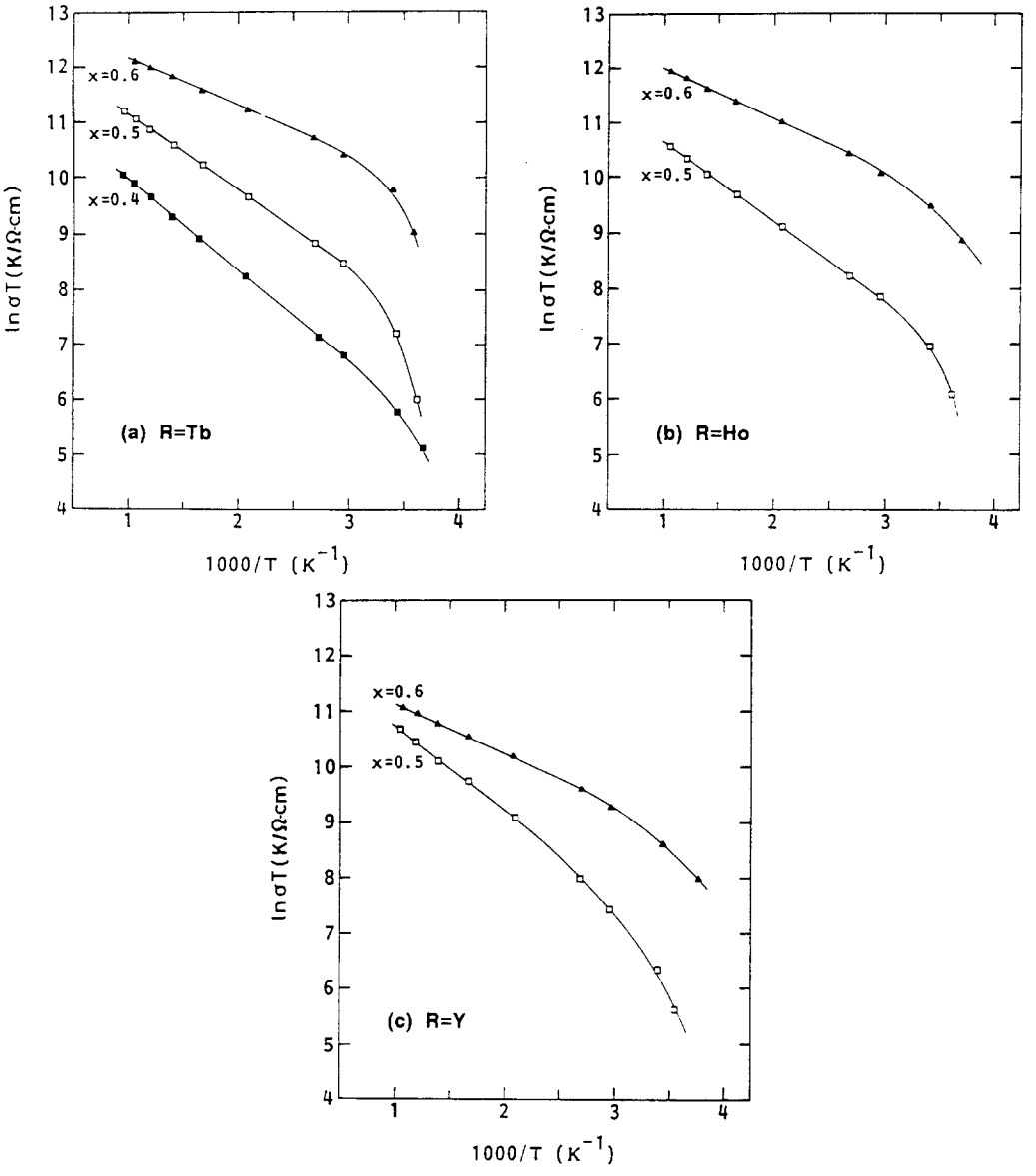

FIG. 5. ln σ T vs $1/T$ plots of $(R_{1-x}Ca_x)MnO_{3-\delta}$ (R: Tb, Ho, Y).

Mott $T^{-1/4}$ law, which indicates the possible occurrence of variable range hopping of electrons due to Anderson localization (*8*, *9*). This conduction mechanism was also proposed for other perovskite systems such as $(R_{1-x}Ca_x)MnO_{3-\delta}$ (R: La, Nd, Gd) (*5–7*) and $(Eu_{1-x}Sr_x)FeO_3$ (*8*).

At higher temperature, the linear relation of ln σ T vs $1/T$ is observed in the composition range $0.4 \leqq x \leqq 0.6$ as shown in Fig. 5, which indicates the occurrence of hopping conduction. Figure 6 shows the relation of ρ vs T of the solid solutions with the composition range $0.7 \leqq x \leqq 0.9$. The sign of

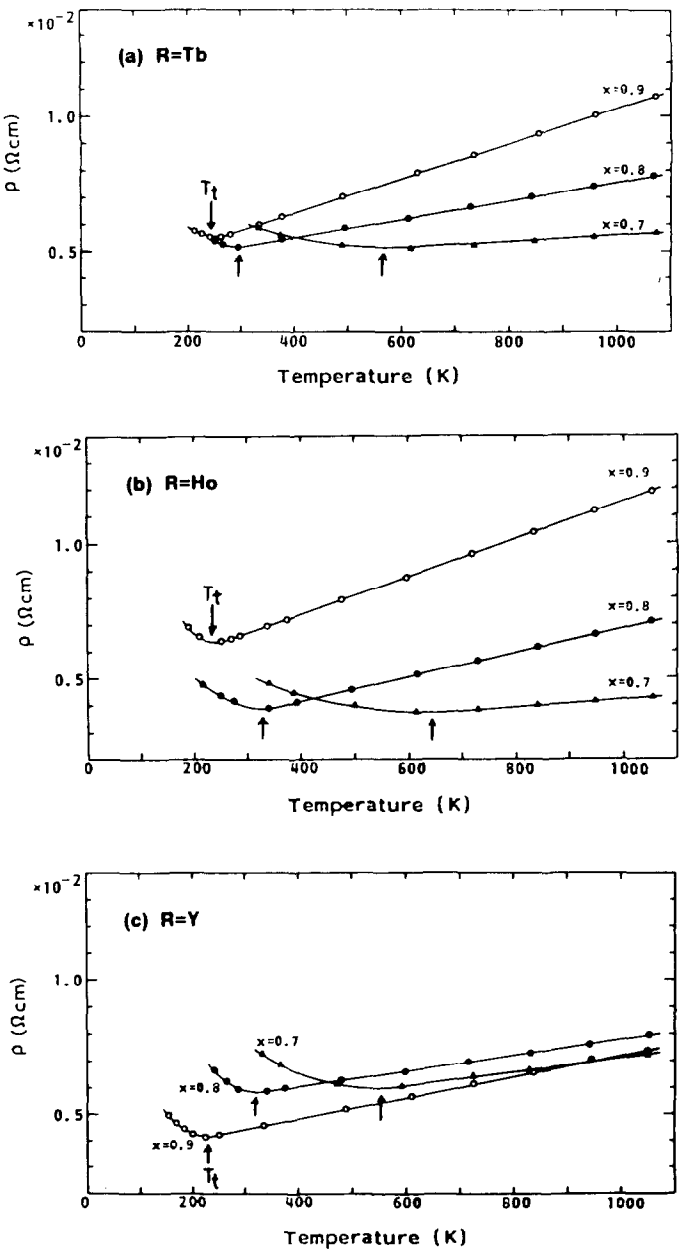

FIG. 6. ρ vs T plots of $(R_{1-x}Ca_x)MnO_{3-\delta}$ (R: Tb, Ho, Y).

$d\rho/dT$ changes from negative to positive and electrical resistivity linearly increases with increasing temperature. From these results, it is obvious that $(R_{1-x}Ca_x)MnO_{3-\delta}$ (R: Tb, Ho, Y, $0.7 \leqq x \leqq 0.9$) exhibits a metal–insulator transition analogous to $(R_{1-x}Ca_x)MnO_{3-\delta}$ (R: La, Nd, Gd) (*5–7*).

Rao and Ganguly (*4*) summarized the metal–insulator transition in some perovskite systems and pointed out that the com-

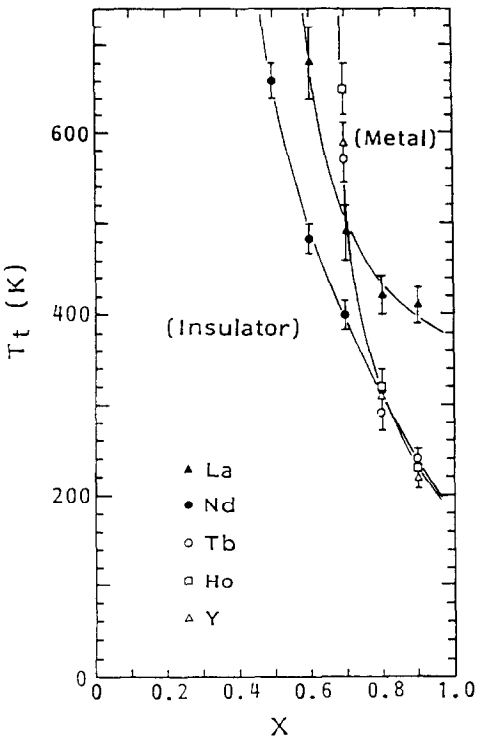

FIG. 7. Metal–insulator transition temperature vs composition in the system $(R_{1-x}Ca_x)MnO_{3-\delta}$ (R: rare earth element).

position-controlled metal–insulator transition occurred at the composition whose value of resistivity was $\sim 2 \times 10^{-3}$ ohm cm. They also pointed out that this critical value of resistivity was close to the value expected from the Mott's concept of minimum metallic conductivity (*15, 16*). It is notable that the metal–insulator transitions in $(R_{1-x}Ca_x)MnO_{3-\delta}$ (R: Tb, Ho, Y, $0.7 \leqq x \leqq 0.9$) occur at the temperature at which the value of resistivity becomes $\sim 5 \times 10^{-3}$ ohm cm. This resistivity value is also close to the Mott's minimum metallic conductivity.

The metal–insulator transition temperature (T_t) is defined as the temperature where the resistivity coefficient changes from negative to positive. The relation between T_t and the composition is shown in Fig. 7, together with the previous works on $(R_{1-x}Ca_x)MnO_{3-\delta}$ (R: La, Nd) (*5, 6*). T_t increases gradually with decreasing x in La^{3+} and Nd^{3+} solid solution systems in which the lattice distortion is small. On the other hand, T_t increases drastically with decreasing x in Tb^{3+}, Ho^{3+}, and Y^{3+} solid solution systems in the composition range where lattice distortion becomes large. This may be due to the variation of the Mn–O interatomic distance with composition.

In order to clarify the relation between T_t and the composition, the Mn–O distance was calculated by using the refined positional parameters of the orthorhombic perovskite-type structure (space group, *Pbnm*) for $(Tb_{1-x}Ca_x)MnO_{2.98}$ ($0.7 \leqq x \leqq 0.9$) and $(Nd_{1-x}Ca_x)MnO_{2.99}$ ($0.5 \leqq x \leqq 0.9$). $(Nd_{1-x}Ca_x)MnO_{2.99}$ samples were prepared as indicated in Ref. (*6*). Structure refinement was carried out by Rietveld analysis of the X-ray powder diffraction data with the "RIETAN" program written by Izumi (*17*). Isotropic thermal parameters were fixed at 0.5 Å^2 for all samples. Final R-factors were all less than 8%. Refined structural parameters and residuals, R_{WP}, R_I and R_F are listed in Table I. R_{WP}, R_I and R_F are the residuals for the weighted pattern, the integrated intensity, and the structure factor, respectively.

Figure 8 shows the relation between T_t and the average Mn–O distance in $(Tb_{1-x}Ca_x)MnO_{2.98}$ and $(Nd_{1-x}Ca_x)MnO_{2.99}$. All the plots well lie on a unique curve. T_t increases with increasing the average Mn–O distance.

The energy band scheme for the perovskite-type structure proposed by Goodenough (*18*) was adopted for the interpretation of the metal–insulator transition in the $(R_{1-x}Ca_x)MnO_{3-\delta}$ (R: La, Nd, Gd) systems (*5–7*). The energy band scheme consists of partially filled σ^* electron and π^* hole states. The localized π^* orbitals of α and β spins at a given cation are split by the interatomic exchange (E_{ex}). Below T_t, electrons exist in the localized π^* orbital of

TABLE I

REFINED STRUCTURAL PARAMETERS FOR $(R_{1-x}Ca_x)MnO_{3-\delta}$ (R: Tb, Nd)

	Space group *Pbnm*				
	Atom	Position	x	y	z
$Tb_{0.1}Ca_{0.9}MnO_{2.98}$	Tb, Ca	4(*c*)	−0.007(2)	0.035(1)	¼
	Mn	4(*b*)	½	0	0
a = 0.5284(1) nm	O(1)	4(*c*)	0.081(5)	0.492(3)	¼
b = 0.5306(1) nm	O(2)	8(*d*)	−0.284(4)	0.293(3)	0.027(3)
c = 0.7475(2) nm					
R_{WP} = 1.66%		R_I = 5.90%		R_F = 6.30%	
$Tb_{0.2}Ca_{0.8}MnO_{2.98}$	Tb, Ca	4(*c*)	−0.005(2)	0.037(1)	¼
	Mn	4(*b*)	½	0	0
a = 0.5296(1) nm	O(1)	4(*c*)	0.097(4)	0.489(3)	¼
b = 0.5328(1) nm	O(2)	8(*d*)	−0.289(4)	0.299(2)	0.024(2)
c = 0.7492(3) nm					
R_{WP} = 1.82%		R_I = 6.20%		R_F = 7.26%	
$Tb_{0.3}Ca_{0.7}MnO_{2.98}$	Tb, Ca	4(*c*)	−0.005(2)	0.039(1)	¼
	Mn	4(*b*)	½	0	0
a = 0.5311(1) nm	O(1)	4(*c*)	0.098(6)	0.493(4)	¼
b = 0.5367(1) nm	O(2)	8(*d*)	−0.295(5)	0.302(3)	0.028(2)
c = 0.7478(2) nm					
R_{WP} = 1.80%		R_I = 4.94%		R_F = 4.80%	
$Nd_{0.1}Ca_{0.9}MnO_{2.99}$	Nd, Ca	4(*c*)	−0.015(2)	0.029(1)	¼
	Mn	4(*b*)	½	0	0
a = 0.5285(1) nm	O(1)	4(*c*)	0.072(7)	0.488(5)	¼
b = 0.5303(1) nm	O(2)	8(*d*)	−0.290(7)	0.284(7)	0.009(6)
c = 0.7475(2) nm					
R_{WP} = 1.98%		R_I = 8.50%		R_F = 7.12%	
$Nd_{0.2}Ca_{0.8}MnO_{2.99}$	Nd, Ca	4(*c*)	−0.010(2)	0.027(1)	¼
	Mn	4(*b*)	½	0	0
a = 0.5306(1) nm	O(1)	4(*c*)	0.100(6)	0.496(6)	¼
b = 0.5330(1) nm	O(2)	8(*d*)	−0.277(7)	0.298(4)	0.011(5)
c = 0.7500(2) nm					
R_{WP} = 1.94%		R_I = 6.37%		R_F = 7.20%	
$Nd_{0.3}Ca_{0.7}MnO_{2.99}$	Nd, Ca	4(*c*)	−0.003(3)	0.027(1)	¼
	Mn	4(*b*)	½	0	0
a = 0.5338(1) nm	O(1)	4(*c*)	0.087(7)	0.493(6)	¼
b = 0.5350(1) nm	O(2)	8(*d*)	−0.286(8)	0.297(6)	0.026(3)
c = 0.7530(2) nm					
R_{WP} = 1.95%		R_I = 5.32%		R_F = 6.33%	
$Nd_{0.5}Ca_{0.5}MnO_{2.99}$	Nd, Ca	4(*c*)	−0.002(3)	0.029(1)	¼
	Mn	4(*b*)	½	0	0
a = 0.5379(1) nm	O(1)	4(*c*)	0.066(8)	0.494(4)	¼
b = 0.5401(1) nm	O(2)	8(*d*)	−0.275(6)	0.306(4)	0.035(3)
c = 0.7591(3) nm					
R_{WP} = 2.00%		R_I = 5.43%		R_F = 5.77%	

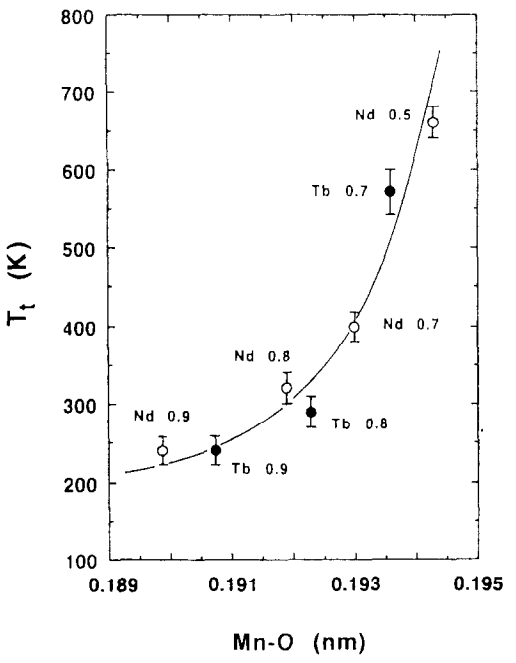

FIG. 8. Metal–insulator transition temperature vs Mn–O distance in the system $(R_{1-x}Ca_x)MnO_{3-\delta}$ (R: Tb, Nd). Numbers in figure correspond to the value of x.

α and β spins. Above T_t, the collective σ^* orbital of α spin overlaps with the localized π^* orbital of β spin. The metal–insulator transition correlates with the magnitude of the electrostatic field (Δ). It is concluded that the increase in Mn–O distance enhances the magnitude of the electrostatic field, and consequently, the metal–insulator transition temperature is raised.

3. Thermoelectric Properties

Figure 9 shows the thermoelectric power of $(R_{1-x}Ca_x)MnO_{3-\delta}$ (R: Tb, Ho, Y) as a function of temperature. In the $(R_{1-x}Ca_x)MnO_{3-\delta}$ (R: Ho, Y, $0.5 \leqq x \leqq 0.9$) systems, the sign of the thermoelectric power is negative; i.e., the major conduction carrier is the electron. The conduction carrier of $(Tb_{1-x}Ca_x)MnO_{2.98}$ is the electron in the composition range $0.5 \leqq x \leqq 0.9$, while that of $(Tb_{1-x}Ca_x)MnO_{2.98}$ with $0.1 \leqq x \leqq 0.4$ is the hole. It is regarded that the conduction carrier is the hole in the case of $Mn^{3+}(3d^4) > (Mn^{4+}(3d^3)$ and it is the electron in the case of $Mn^{3+} < Mn^{4+}$, when hopping or metallic conduction occurs in the mixed valency oxides containing Mn ions. This aspect is also applied to the present solid solution systems.

Since $(R_{1-x}Ca_x)MnO_{3-\delta}$ (R: Tb, Ho, Y, $0.7 \leqq x \leqq 0.9$) solid solutions possess large thermoelectric power and high electrical conductivity in the metallic conduction region, they are considered to be candidates as high temperature thermoelectric conversion materials. The figure of merit (Z) of thermoelectric conversion was calculated by the equation $Z = S^2\sigma/\lambda$, where S, σ, and λ are thermoelectric power, electrical conductivity, and thermal conductivity, respectively. Here, the value of λ was taken from the data of another orthorhombic perovskite, $LaCrO_3$, given by Weber *et al.* (*19*). Results are shown in Fig. 10. Z mainly depends on the thermoelectric power, because the electrical conductivity of all samples is about 10^2 (S/cm) in the metallic conduction region. Figure 11 shows the figure of merit of $(R_{1-x}Ca_x)MnO_{3-\delta}$ (R: Tb, Ho, Y) together with various commercial used thermoelectric materials (*20*). Z values of the present solid solution systems are lower than those of other representative thermoelectric materials by an order of magnitude, but they become slightly higher than that of β-$FeSi_2$ above 800°C, suggesting the possible application for high temperature thermoelectric conversion.

Conclusion

In the present study, solid solutions $(R_{1-x}Ca_x)MnO_{3-\delta}$ (R: Tb, Ho, Y), with the orthorhombic perovskite-type structure were synthesized by solid state reactions. Two types of orthorhombic structures, the O-type and the O′-type, are found in these systems. The boundary of the tolerance fac-

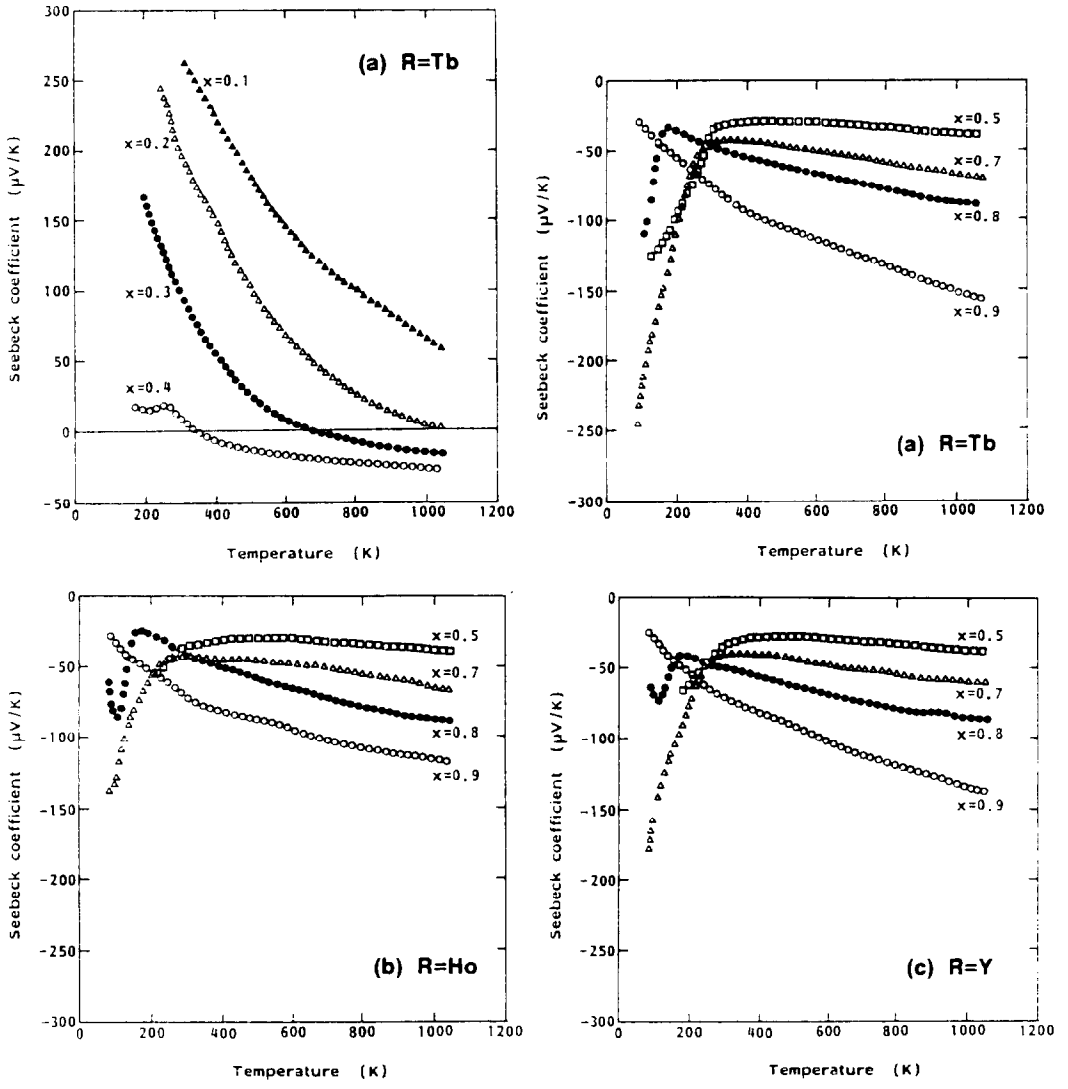

FIG. 9. Temperature dependence of the thermoelectric power of $(R_{1-x}Ca_x)MnO_{3-\delta}$ (R: Tb, Ho, Y).

tor between the O-type and the O′-type is determined to be 0.860.

The conduction mechanism in $(R_{1-x}Ca_x)MnO_{3-\delta}$ (R: Tb, Ho, Y) systems is explained by variable range hopping of electrons due to Anderson localization in the low temperature region. At high temperature, the metal–insulator transition occurs in the composition range $0.7 \leqq x \leqq 0.9$. Transition temperature increases with increasing average Mn–O distance. This fact is interpreted by an enhancement of the magnitude of the electrostatic field in the energy band scheme (*18*) with increasing Mn–O distance.

$(R_{1-x}Ca_x)MnO_{3-\delta}$ (R: Tb, Ho, Y, $0.7 \leqq x \leqq 0.9$) have large thermoelectric power and high electrical conductivity in the metallic conduction region. These materials are con-

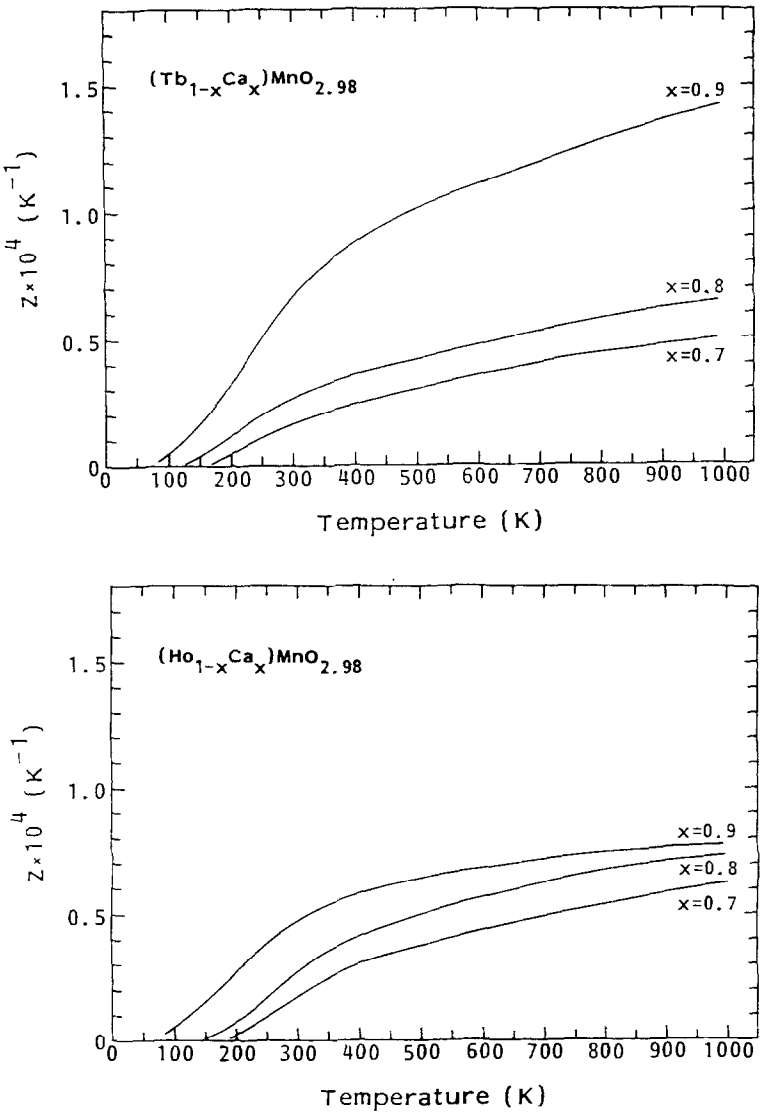

FIG. 10. Figure of merit (Z) vs temperature of $(R_{1-x}Ca_x)MnO_{3-\delta}$ (R: Tb, Ho, Y).

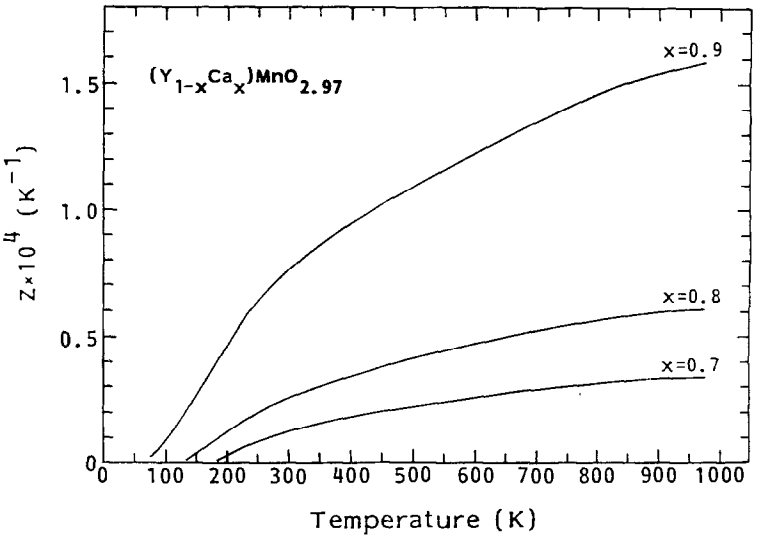

FIG. 10—*Continued*

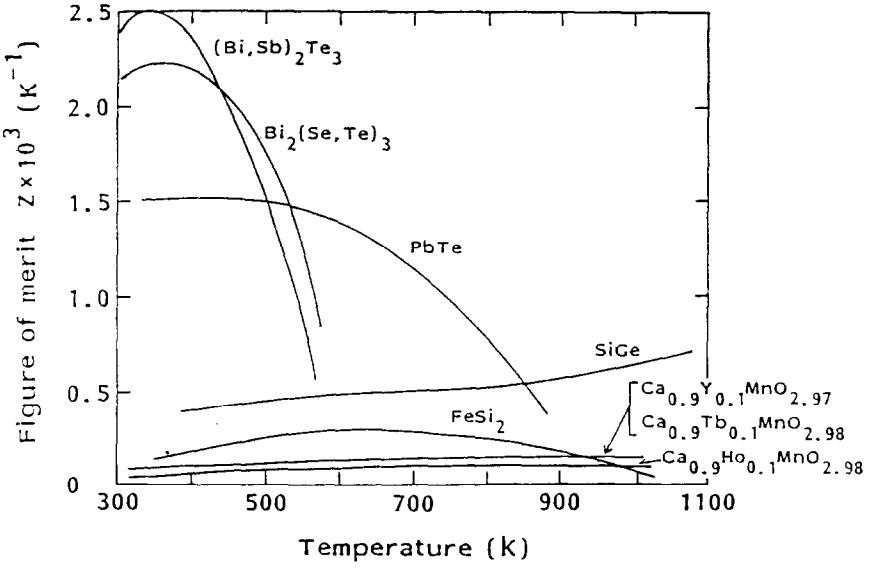

FIG. 11. Figure of merit (Z) vs temperature of various thermoelectric materials.

sidered to be candidates as high temperature thermoelectric conversion materials.

Acknowledgment

This work has been supported in part by a Grant-in-Aid for Scientific Research on Priority Areas for Energy Conversion and Utilization with High Efficiency of the Ministry of Education, Science and Culture.

References

1. C. N. R. Rao, V. G. Bhide, and N. F. Mott, *Philos. Mag.* **32,** 1277 (1975).
2. C. N. R. Rao and Om Parkash, *Philos. Mag.* **35,** 1111 (1977).
3. P. Ganguly, N. Y. Vasanthacharya, C. N. R. Rao, and P. P. Edwards, *J. Solid State Chem.* **54,** 400 (1984).
4. C. N. R. Rao and P. Ganguly, *in* "Metallic and Non-metallic States of Matter" (P. P. Edwards and C. N. R. Rao, Eds.), p. 329, Taylor and Francis, London (1985).
5. H. Taguchi and M. Shimada, *J. Solid State Chem.* **63,** 290 (1986).
6. H. Taguchi, M. Nagao, and M. Shimada, *J. Solid State Chem.* **76,** 284 (1988).
7. H. Taguchi, M. Nagao, and M. Shimada, *J. Solid State Chem.* **82,** 8 (1989).
8. V. Joshi, O. Parkash, G. N. Rao, and C. N. R. Rao, *J. Chem. Soc. Faraday Trans. 2* **75,** 1199 (1979).
9. N. F. Mott, *Adv. Phys.* **21,** 785 (1972).
10. B. E. Gushee, L. Katz, and R. Ward, *J. Am. Chem. Soc.* **79,** 5601 (1957).
11. H. Taguchi and M. Shimada, *J. Solid State Chem.* **67,** 37 (1987).
12. V. M. Goldschmidt, *Akad. Oslo I, Mat.-Natur.*, No. 2, 7 (1926).
13. L. H. Ahrens, *Geochim. Cosmochim. Acta* **2,** 155 (1952).
14. E. Pollert, S. Krupička, and E. Kuzmičová, *J. Phys. Chem. Solids* **43,** 1137 (1982).
15. N. F. Mott, *J. Non-Cryst. Solids* **1,** 1 (1968).
16. N. F. Mott, *Philos. Mag. B,* **44,** 265 (1981).
17. F. Izumi, *Nippon Kessho Gakkaishi,* **27,** 23 (1985). [in Japanese]
18. J. B. Goodenough, *J. Appl. Phys.* **37,** 1415 (1966).
19. W. J. Weber, C. W. Griffin, and J. L. Bates, *J. Am. Ceram. Soc.* **70,** 265 (1987).
20. I. Nishida, *Kogyo Zairyo* **33**(4), 108 (1985). [in Japanese]